Geophysical Research Letters

RESEARCH LETTER
10.1029/2021GL095655

Connection Between Foreshock Structures and the Generation of Magnetosheath Jets: Vlasiator Results

J. Suni[1], M. Palmroth[1,2], L. Turc[1], M. Battarbee[1], A. Johlander[1,3], V. Tarvus[1], M. Alho[1], M. Bussov[1], M. Dubart[1], U. Ganse[1], M. Grandin[1], K. Horaites[1], T. Manglayev[1], K. Papadakis[1], Y. Pfau-Kempf[1], and H. Zhou[1]

[1]Department of Physics, University of Helsinki, Helsinki, Finland, [2]Space and Earth Observation Centre, Finnish Meteorological Institute, Helsinki, Finland, [3]Swedish Institute of Space Physics, Uppsala, Sweden

Key Points:

- We investigated magnetosheath jets in four hybrid-Vlasov simulation runs with different solar wind parameters
- Foreshock compressive structures can explain the formation of up to 75% of magnetosheath jets
- The foreshock compressive structure-caused jets travel deeper into the magnetosheath than the 25% of the jets whose origins remain unclear

Supporting Information:

Supporting Information may be found in the online version of this article.

Correspondence to:

J. Suni,
jonas.suni@helsinki.fi

Citation:

Suni, J., Palmroth, M., Turc, L., Battarbee, M., Johlander, A., Tarvus, V., et al. (2021). Connection between foreshock structures and the generation of magnetosheath jets: Vlasiator results. *Geophysical Research Letters*, *48*, e2021GL095655. https://doi.org/10.1029/2021GL095655

Received 11 AUG 2021
Accepted 2 OCT 2021

Abstract Earth's magnetosheath consists of shocked solar wind plasma that has been compressed and slowed down at the Earth's bow shock. Magnetosheath jets are pulses of enhanced dynamic pressure in the magnetosheath. Jets have been observed by numerous spacecraft missions, but their origin has remained unconfirmed, though several formation mechanisms have been suggested. In this study, we use a method for automatically identifying and tracking jets as well as foreshock compressive structures (FCSs) in four 2D runs of the global hybrid-Vlasov simulation Vlasiator. We find that up to 75% of magnetosheath jets are caused by FCSs impacting the bow shock. These jets propagate deeper into the magnetosheath than the remaining 25% of jets that are not caused by FCSs. We conduct a visual case study of one jet that was not caused by FCSs and find that the bow shock was not rippled before the formation of the jet.

Plain Language Summary The space around Earth is filled with plasma, the fourth state of matter. Earth's magnetic field shields our planet from the stream of plasma coming from the Sun, the solar wind. The solar wind plasma is slowed down at the Earth's bow shock, before it flows against and around the Earth's magnetic field in the magnetosheath. Sometimes, pulses of high density or velocity can occur in the magnetosheath that have the potential to disturb the inner regions of near-Earth space where many spacecraft orbit. We call these pulses magnetosheath jets. Magnetosheath jets have been observed by many spacecraft over the past few decades, but how they form has remained unclear. In this study, we use the Vlasiator model to simulate plasma in near-Earth space and investigate the origins of magnetosheath jets. We find that the formation of up to 75% of these jets can be explained by compressive structures in the foreshock, a region populated by intense wave activity extending sunward of the quasi-parallel bow shock, where interplanetary magnetic field lines allow shock-reflected particles to travel back toward the Sun.

1. Introduction

Earth's magnetosheath forms the interface between our planetary magnetosphere and the supermagnetosonic solar wind flow. The magnetosheath is bounded by the bow shock separating it from the upstream solar wind, and by the magnetopause, which is the outer boundary of the magnetosphere. An important factor determining the nature of the bow shock and the magnetosheath is the orientation of the interplanetary magnetic field (IMF). Where the bow shock normal direction is quasi-parallel to the IMF, solar wind particles reflected at the bow shock can stream back toward the Sun, forming the turbulent foreshock upstream of the shock (e.g., Eastwood et al., 2005; Hoppe et al., 1981). Consequently, the magnetosheath behind the quasi-parallel bow shock is more turbulent (e.g., Dimmock et al., 2014; Gutynska et al., 2015) than the quasi-perpendicular magnetosheath. In recent years, one of the most important avenues in magnetosheath research has been the study of magnetosheath jets (e.g., Plaschke et al., 2018), which are regions of high dynamic pressure. Magnetosheath jets are widely associated with the quasi-parallel magnetosheath (Archer & Horbury, 2013; Němeček et al., 1998; Plaschke et al., 2013; Vuorinen et al., 2019), suggesting that their origin is tied to the interactions between the foreshock and the bow shock. Results from global hybrid simulations (Karimabadi et al., 2014; Omelchenko et al., 2021; Omidi et al., 2016; Palmroth, Hietala, et al., 2018) likewise point to foreshock–bow shock interaction as the origin of jets.

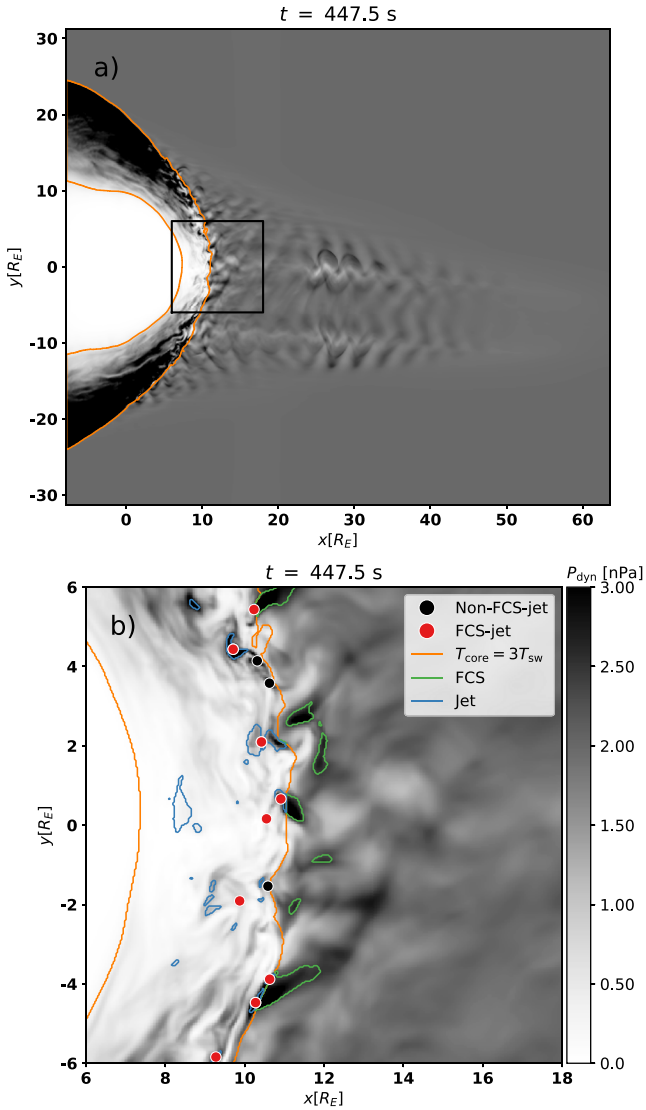

Figure 1. (a) View of the entire spatial domain of run HM05 at 447.5 s from the start of the simulation. The background color shows the dynamic pressure. (b) Zoom-in to the subsolar magnetosheath and foreshock delineated by the black box in panel (a) The foreshock compressive structure (FCS) magnetic threshold is $\eta = 1.5$. The orange contours show the boundaries of compressed and heated plasma, representing the bow shock and magnetopause. The green (blue) contours delineate the FCS (jet) regions. The red dots mark the centers of FCS-jets. The black dots mark the centers of non-FCS-jets. Unmarked jet regions did not originate at the bow shock. Movie S1 shows the time-evolution of panel (b).

Several suggestions have been made to explain the formation of magnetosheath jets. Archer et al. (2012) proposed that jets are caused by solar wind pressure pulses or rotational discontinuities. Hietala et al. (2009) suggested a mechanism in which a local ripple in the quasi-parallel bow shock could lead to the refraction and funneling of plasma, such that the dynamic pressure increases across the shock. Karlsson et al. (2015) associated jet-like "paramagnetic plasmoids" with short large-amplitude magnetic structures (SLAMS), which are steepened foreshock fluctuations having a high dynamic pressure and magnetic field (Lucek et al., 2002, 2004). A statistical study of spacecraft data by Raptis et al. (2020) found evidence for both the bow shock ripple mechanism and the SLAMS mechanism. The problem with trying to prove these theories based on observations is that the spacecraft are seldom, if ever, in a suitable array such that both the production mechanism and the resulting jet can simultaneously be identified unambiguously, and therefore the origin of jets is still controversial (see Plaschke et al., 2018). Partly due to this problem, Palmroth, Hietala, et al. (2018) studied an individual jet using an ion-kinetic global simulation Vlasiator, and found that the studied jet was essentially a SLAMS propagating through the magnetosheath, in agreement with Karlsson et al. (2015). However, since this investigation concerned only one carefully validated jet, the origin of jets in general was still not addressed.

In this study, we will quantify the proportion of magnetosheath jets that are unambiguously associated with foreshock structures. We will also study the differences between jets that are associated with foreshock structures and jets that are not, as well as investigate the formation of jets that are not associated with foreshock structures. The goal is to gain a better understanding of jet formation in general and the SLAMS mechanism in particular.

2. Model and Methods

The global hybrid-Vlasov simulation Vlasiator (Palmroth, Ganse, et al., 2018) models protons as distribution functions, while electrons are treated as a massless charge-neutralizing fluid. The time-evolution of the proton distribution functions is governed by the Vlasov equation, while the electromagnetic fields obey Maxwell's equations as well as Ohm's law including the Hall term. Vlasiator is 6-dimensional (6D), with 3 dimensions for real space, and 3 for velocity space. The four simulation runs investigated in this study, presented also in Palmroth et al. (2021), neglect the third real space dimension in order to limit the computational cost of the simulations, and are therefore carried out in the Geocentric Solar Ecliptic (GSE) xy plane. The simulation boxes of all four runs are large enough to capture the solar wind, foreshock, dayside magnetosheath and partially the nightside (see Figure 1a for one of the runs used here). The outer boundaries of the simulation box are periodic in the out-of-plane direction, in y and $-x$ boundaries apply Neumann conditions, while the solar wind flows in with constant parameters from the $+x$ boundary together with an in-plane IMF. The inner boundary of the magnetosphere is the same for all runs, a perfect conductor at 5 R_E from the origin. The solar wind parameters for the four runs are described in Table 1. The solar wind speeds were chosen to be relatively fast so as to accelerate the development of the bow shock and magnetosheath and thus save computational resources. The most important parameter for the realistic evolution of the system, however, is the Alfvén Mach number, which in our runs are within the normal range of observations at Earth (Winterhalter & Kivelson, 1988).

Table 1
Properties of the Different Runs Used in the Study

Run	$\mathbf{B}_{\mathrm{IMF}}$ [nT]	$\lvert\mathbf{B}_{\mathrm{IMF}}\rvert$ [nT]	Cone angle [°]	n [cm^{-3}]	v_x [kms^{-1}]	M_{A}	Search box [R_{E}]	Tracking duration [s]	#Jets
HM30	(−4.3,2.5,0)	5	30	1	−750	6.9	(6,18,−8,6)	129.5	128
HM05	(−5.0,0.4,0)	5	5	3.3	−600	10	(6,18,−6,6)	299.5	273
LM30	(−8.7,5.0,0)	10	30	1	−750	3.4	(6,18,−8,6)	379.5	380
LM05	(−10.0,0.9,0)	10	5	3.3	−600	5	(6,18,−6,6)	149.5	177

Note. From left to right, the columns give the run identifier, IMF vector in GSE, IMF strength, IMF cone angle, solar wind number density, solar wind velocity, solar wind Alfvén Mach number, search box ($x_{\min}, x_{\max}, y_{\min}, y_{\max}$), jet tracking duration, and total number of jets found in the run. For all runs, the solar wind temperature is 0.5 MK, the real space resolution is 227 km, and the velocity space resolution is 30 kms^{-1}.

Figure 1b shows an example of the foreshock-magnetosheath region in one of the runs (HM05, see Table 1). The foreshock is on the right, and the boundaries of compressed and heated plasma, indicating the bow shock and the magnetopause and shown with orange contours, are defined by the ion core population heating criterion $T_{\mathrm{core}} = 3T_{\mathrm{sw}}$ after Battarbee et al. (2020) and Wilson et al. (2014). Jets, delineated with blue and marked with red or black dots in Figure 1b, are defined as structures in the magnetosheath that originated at the bow shock and fulfill the Archer and Horbury (2013) jet criterion, $P_{\mathrm{dyn}} \geq 2\langle P_{\mathrm{dyn}}\rangle_{3\mathrm{min}}$, similarly as in Palmroth et al. (2021). That is, the instantaneous dynamic pressure should be at least twice its 3-min time average.

In this study, we investigate the relationship between jets and foreshock structures, and therefore we define here the concept of foreshock compressive structures (FCSs), which encompasses various kinds of magnetic structures. FCSs, delineated with green in Figure 1b, are defined as structures upstream of the bow shock that fulfill $P_{\mathrm{dyn}} \geq 1.2P_{\mathrm{dyn,sw}}$ and $\lvert\mathbf{B}\rvert \geq \eta\,\lvert\mathbf{B}_{\mathrm{IMF}}\rvert$. The dynamic pressure condition is used to ensure that the upstream edge of the bow shock where the magnetic field strength ramps up is not accidentally detected as a single FCS. The value 1.2 is chosen to be high enough to achieve this, but small enough not to bias the FCS detection toward only compressive structures with highly enhanced dynamic pressure. We vary the threshold parameter η in this study. In Figures 1b and 1a threshold value of $\eta = 1.5$ is used. Movie S1 shows FCSs, jets and the boundaries of compressed and heated plasma for the tracking duration of run HM05.

In order to understand the interconnection of FCSs and jets statistically, we carried out a search of jets and FCSs in all four runs shown in Table 1. We restricted the search domains to regions where they are most likely to exist (see Table 1), while still capturing as much as possible of the foreshock and quasi-parallel magnetosheath, focusing on the region close to the nose of the bow shock and omitting the flanks, as the magnetosheath flow accelerates to super-Alfvénic tailward velocities at the flanks and it is thus unlikely for jets that propagate toward the magnetopause to form there. Jet and FCS tracking began when the simulations had properly initialized at $t = 290$ s in all runs and ended after the duration specified by the "tracking duration," which varies between runs because of different run durations. The search of jets and FCSs is carried out by delineating from the simulation the regions which fulfill either the jet or FCS criteria, and giving each region an identity. Two regions are considered distinct if they are separated by a gap of at least two simulation cells. Regions are tracked across time by studying the overlap of the individual regions identified at successive simulation time steps. Two regions identified during two successive time steps that share at least 50% of the cells of the smaller region are considered to be the same. If a region disappears and another overlapping one reappears within 2.5 s, they are considered the same individual region. The reappearance time is chosen manually to avoid double counting structures. This identification algorithm is essentially the same as used for jets only in Palmroth et al. (2021), except that we require that jets start at the bow shock. This is done because Palmroth et al. (2021) posited that regions forming deeper in the magnetosheath are not actually jets but rather momentary fluctuations in the magnetosheath properties that fulfill the jet criteria. A jet is considered attached to the bow shock if the gap between the jet region and the upstream region is at most one cell. For this purpose, the upstream is defined as the region where either the ion core population temperature is $T_{\mathrm{core}} < 3T_{\mathrm{sw}}$ or the magnetosonic Mach number is $M_{\mathrm{ms},x} \geq 1$ (Battarbee

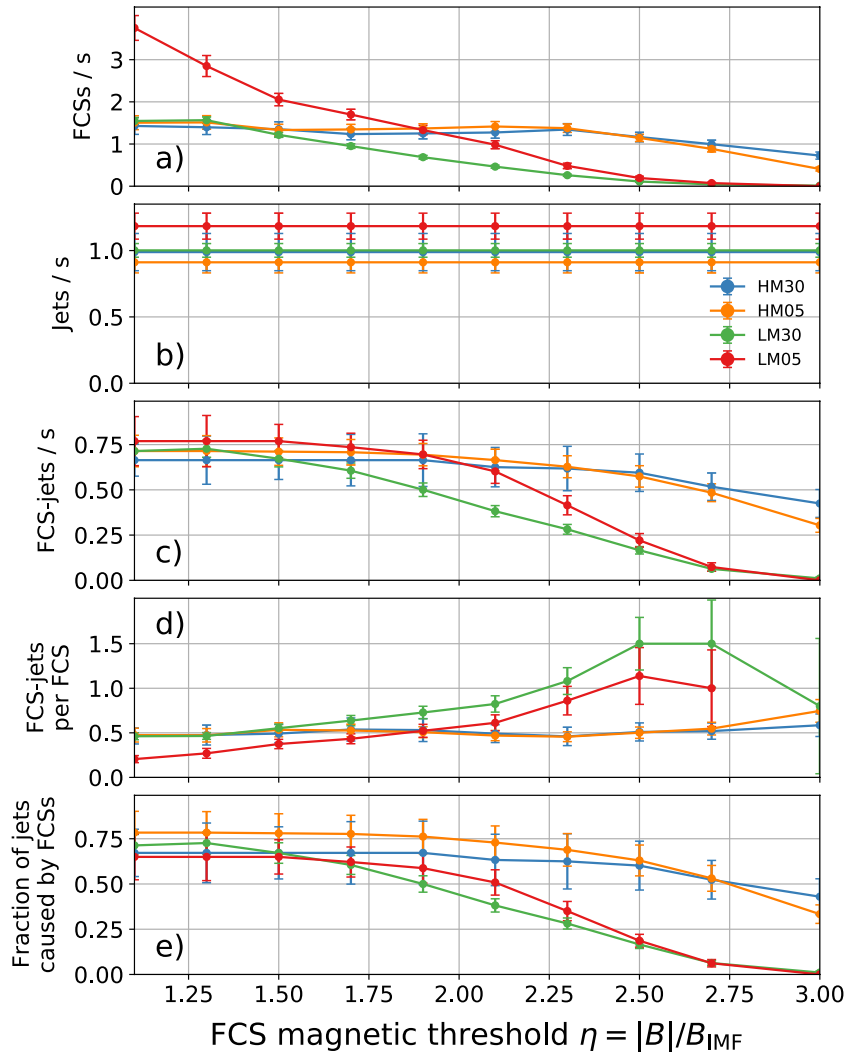

Figure 2. Jet and foreshock compressive structure (FCS) statistics as a function of FCS magnetic threshold: (a) FCS appearance frequency, (b) jet appearance frequency, (c) FCS-jet appearance frequency, (d) ratio of FCS-jets to FCSs, and (e) fraction of jets caused by FCSs. Different runs are given with different colors (see text). The error bars show the standard errors.

et al., 2020). Finally, the jets are divided into two categories: FCS-jets, which at any point in their lifetime come within two cells of an FCS region, and non-FCS-jets, which do not. The total number of jets found in each run is given in Table 1.

3. Results

While there are well-established criteria to identify magnetosheath jets, for example, Archer and Horbury (2013), this is not the case for foreshock structures. Therefore, in the following analysis we treat the FCS threshold η as a variable. For reference, many studies require thresholds of $\delta B/B_0 \geq 2$, which corresponds to $\eta \geq 3$, for a structure to be a SLAMS (e.g., Schwartz et al., 1992), whereas, for example, Lucek et al. (2008) define $\delta B/B_0 \geq 1$ ($\eta \geq 2$). Figure 2 shows the number of FCSs, jets, and FCS-jets as a function of the FCS magnetic threshold (the dynamic pressure threshold is constant at 1.2 times the solar wind value). The different runs in Table 1 are given as different colors such that blue (green) corresponds to a solar wind Alfvén Mach number M_A of 6.9 (3.4) and a 30° IMF cone angle measured from the Sun-Earth line, while orange (red) corresponds to solar wind Alfvén Mach number 10 (5) and a 5° IMF cone angle.

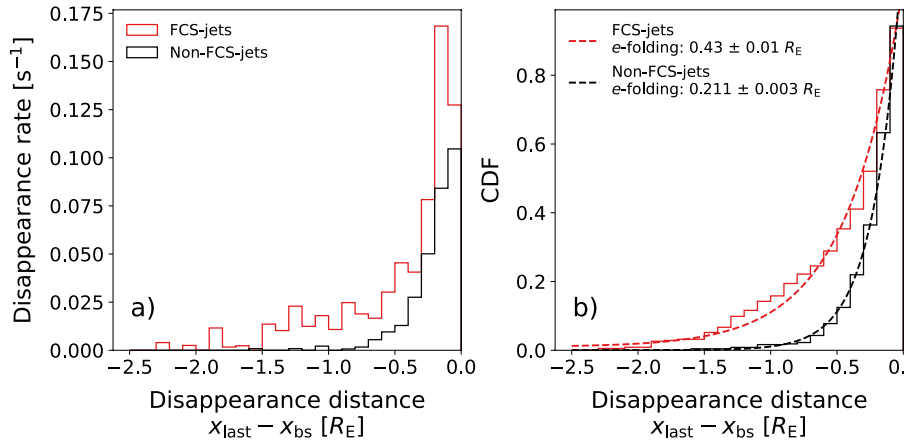

Figure 3. Histograms of jet disappearance location downstream of the bow shock with foreshock compressive structures magnetic threshold $\eta = 1.5$: (a) Number of jets per second disappearing at different distances from the bow shock, and (b) the cumulative distribution function of the disappearance distances, indicating the probability of a jet propagating to a given distance. The e-folding distances are acquired by fitting exponential regression models (dashed curves) to the cumulative distribution functions.

Figure 2a shows the number of FCSs forming in each run normalized by the corresponding tracking duration (see Table 1), giving the rate at which new FCSs appear in the foreshock. At low values of η, many small and low-amplitude structures are identified as FCSs, causing the number of FCSs to be larger than at high threshold values. For the low M_A runs, the number of FCSs decreases with rising η, whereas for high M_A runs the number remains mostly constant irrespective of η, indicating that all the FCSs there have relatively high amplitudes. Figure 2b shows the average rate of appearance of new jets in each run. As the jet criteria do not depend on the FCS magnetic threshold, this is a constant for each run.

Figure 2c shows the appearance rate of jets that are connected to an FCS during their lifetime (see Section 2), while Figure 2d shows the ratio of FCS-related jets to FCS (panel c divided by panel a). For high M_A, this is effectively constant, while for low M_A the ratio increases with increasing η, although in these cases the absolute number of FCSs at high η is low. The ratio is undefined for $\eta = 3$ in run LM05, as there are no FCSs in the run for this threshold value. Figure 2e shows the fraction of jets that are connected to an FCS during their lifetime (panel c divided by panel b). For η up to about 1.5, this fraction is almost a constant at 0.75. In the following analysis, we will use a threshold value of $\eta = 1.5$, as it is sufficiently high to retain only structures that are significantly compressive, while also keeping a large number of structures (958 jets and 1,343 FCSs across all runs). We discuss this threshold in Section 4.

Next, we study the difference between FCS-jets and non-FCS-jets. Figure 3a shows the average over the 4 simulation runs of the disappearance rates of FCS-jets and non-FCS-jets that start at the bow shock as a function of distance from the bow shock. Figure 3b shows the cumulative distribution function (CDF) of the disappearance distances of the jets in Figure 3a. This roughly corresponds to the probability of detecting a jet at a certain distance from the bow shock. For defining the jet distance from the bow shock, the position of the shock x_{bs} is determined by a fifth-degree polynomial fit of the coordinates of the cells at the bow shock defined by the core heating criterion. Figure 3 shows that both FCS-related jets and non-FCS-jets mostly disappear close to the bow shock shortly after forming, but a larger fraction of FCS-jets penetrate deeper into the magnetosheath compared to non-FCS-jets. By fitting exponential functions to the CDFs in Figure 3b, the e-folding distance can be calculated to be $0.43 \pm 0.01\ R_E$ for FCS-jets and $0.211 \pm 0.003\ R_E$ for non-FCS-jets. We fit the exponential function, similarly to Plaschke et al. (2016), in order to quantitatively study the penetration of jets into the magnetosheath. In Section 4, we use the e-folding distance to estimate the magnetopause impact rate in a way that can be compared to the results obtained by Plaschke et al. (2016, 2020).

As Figure 2 shows that about 75% of all jets are associated with (low-magnitude) FCSs in all runs, it is interesting to briefly contemplate the causes of the remaining 25% of the jets. Figure 4 shows snapshots of run HM05 with $\eta = 1.5$, where we visually inspect one representative non-FCS-jet at approximately $(x, y) =$

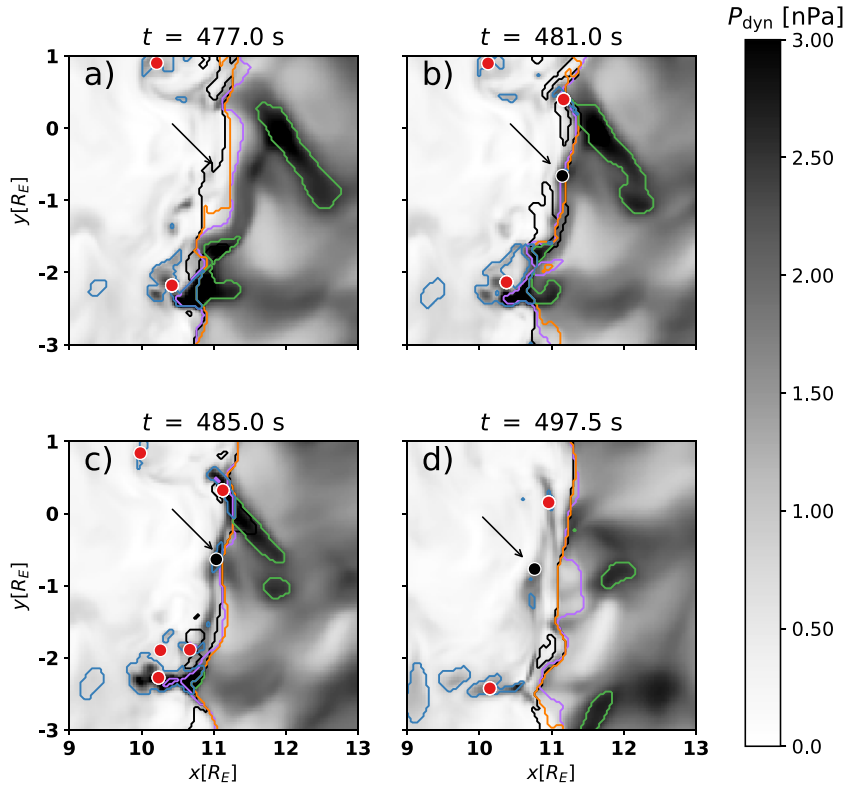

Figure 4. Snapshots of Movie S2 of run HM05 at (a) 477.0, (b) 481.5, (c) 485.0, and (d) 497.5 s from the start of the simulation, investigating the formation of the non-FCS-jet at $(x, y) = (11.25, -0.6)$ R_E in panel (b) Contours and dots are as in Figure 1b, with two additional bow shock contours: The $M_{ms,x}$ criterion (violet) and the density criterion (black, see details in Section 3).

(11.25, −0.6) R_E, indicated by the black arrow. In addition to the orange contour at $T_{core} = 3T_{sw}$, two other definitions described by Battarbee et al. (2020) for the bow shock position are used in Figure 4: $n = 2n_{sw}$ (black) and $M_{ms,x} = 1$ (violet). In Figure 4a, at the location where the non-FCS-jet later forms, the three different estimations of the bow shock boundary do not agree with each other, that is, the bow shock is non-local (a metric introduced in Battarbee et al., 2020), but there is no nearby indentation of the shock that would indicate formation through the mechanism suggested by Hietala et al. (2009). An indentation of the bow shock can be seen at $y = -2$ R_E, but this indentation has an FCS upstream of it and an FCS-jet downstream of it. In Figure 4b, the non-FCS-jet has formed, and the bow shock behind it is neither indented nor non-local. Figure 4c shows that the properties of the bow shock have not changed significantly behind the non-FCS-jet. In Figure 4d, the non-FCS-jet is shown at the last point in its lifetime. Movie S2 shows FCSs, jets, and the three bow shock contours in the same box as Figure 4 for each time step in a time interval around the lifetime of this non-FCS-jet.

4. Discussion

The FCS magnetic threshold value of $\eta = 1.5$ represents a transition point, below which the fraction of jets caused by FCSs no longer significantly increases, and above which the fraction starts decreasing. Rojas-Castillo et al. (2013) suggest that the lower limit of magnetic enhancement for nonlinear compressive structures in the foreshock is around $\delta B/B_0 = 40\%$, which corresponds to $\eta = 1.4$. As seen in Figure 2, for low M_A the fraction starts decreasing rapidly around this threshold value due to the lack of strongly compressive structures in the foreshock, while for high M_A the fraction decreases more slowly, and remains nearly constant until a threshold of approximately $\eta = 2.3$. Lucek et al. (2008) suggest that $\eta \approx 2$ represents the lower limit of magnetic enhancement for SLAMS. The differences in behavior between the low-M_A and high-M_A simulation runs suggest that the amplitude of magnetic enhancements in the foreshock is smaller during

low-M_A solar wind conditions, and the large FCS occurrence rate at low magnetic thresholds in run LM05 is in agreement with the fact that the foreshock structures have smaller spatial extents and the foreshock waves have lower amplitudes and higher frequencies during high-$|B|$ and thus low-M_A conditions (Turc et al., 2018). The lower amplitudes and higher frequencies of the initial waves probably prevent the FCSs in the low-M_A runs from growing large enough in amplitude to be detected at higher values of η, which would explain the lack of FCSs for $\eta = 3$ in run LM05. Figure 4 shows that bow shock indentation or rippling, suggested by Hietala et al. (2009), was not responsible for the formation of the studied non-FCS-jet, but indentation was present during the formation of an FCS-jet. As can be seen in Movie S2, when the FCS at $y = -2\ R_E$ approaches the bow shock, the supermagnetosonic plasma associated with the FCS indents the bow shock and contributes to the formation of the FCS-jet. The compressive magnetic structure of the FCS, however, slows down and steepens, causing shock reformation to be visible in the density contour. This is consistent with the patchwork model of the bow shock described by Schwartz et al. (1992). The use of steady input for the solar wind and IMF also rules out solar wind discontinuities (Archer et al., 2012) as the source of the non-FCS-jet.

Comparing the occurrence rate of jets (Figure 2b) to studies based on spacecraft observations is difficult, as the methods used for determining the rate are vastly different. Plaschke et al. (2016) report that the rate at which the jets impact the magnetopause is approximately 2.90 large jets/hour, while Plaschke et al. (2020) find that this rate for jets with perpendicular sizes smaller than 1 R_E can be roughly 20–1,000 jets/hour. The jet extents in the Vlasiator runs are of the order of 1 R_E or smaller (Palmroth et al., 2021). While Figure 2 indicates that the jet occurrence rate in this study is on average ~1 jet/second, only a fraction of them impact the magnetopause. Assuming a sheath thickness of ~2 R_E (Figure 3) and that FCS-jets account for ~75% of all forming jets (Figure 2e), we can use the e-folding distances from Figure 3b to estimate the magnetopause impact rate: 26 FCS-jets/hour and 0.069 non-FCS-jets/hour. The rate for FCS-jets is roughly comparable to the lower limit of small jets in Plaschke et al. (2020). The 2D set-up of our simulations results in enhanced magnetic pile-up in front of the magnetopause, which in turn can form a magnetic barrier preventing the jets from reaching the magnetopause, as well as making the magnetosheath thicker than in 3D. This could explain the relatively low impact rate. Our impact rate estimate is also only for the GSE xy plane, so the actual rate could be higher. On the other hand, the 2D set-up also prevents jets from dissipating in the out-of-plane direction, possibly making them live longer and propagate deeper into the magnetosheath.

5. Conclusions

In this study, we have carried out a comprehensive statistical survey of the association of magnetosheath jets to FCSs using the Vlasiator ion-kinetic simulation. We tracked the FCSs within the foreshock using an automatic algorithm, and gave them an identity in time. At the bow shock, we find that up to 75% of the forming jets are caused by FCSs. The remaining 25% of the jets appear to be caused by some other mechanism. Based on Movies S1 and S2, one can even state that the FCSs are continually transformed into jets at the bow shock. We conclude that a clear majority of jets are caused by FCSs, in accordance with Karlsson et al. (2015) and Palmroth, Hietala, et al. (2018). We also conclude that the FCS-jets propagate around twice as far into the magnetosheath compared to non-FCS-jets.

In conclusion, our numerical simulations suggest that FCSs impacting the bow shock can explain the formation of the majority of magnetosheath jets, but not all. FCS-jets and non-FCS-jets appear to have somewhat different properties, supporting the possibility that that they might be formed through different mechanisms. Visual inspection of the formation of a non-FCS-jet reveals nothing conclusive about the formation of non-FCS-jets, but the presence of shock reformation and non-locality at the formation site suggest a possible connection between these phenomena and jet formation. This is to be investigated in a future study.

Data Availability Statement

Vlasiator is distributed under the GPL-2 open-source license. Vlasiator uses a data structure developed in-house. The Analysator software (Battarbee et al., 2021) was used to produce the presented figures. The runs described here can be either run with the above-mentioned code using the boundary conditions reported in

this paper, or the data sets can be downloaded from the University of Helsinki servers where they are stored (Pfau-Kempf et al., 2021b).

Acknowledgments
The authors acknowledge the European Research Council for starting grant 200141-QuESpace, with which Vlasiator (Pfau-Kempf et al., 2021a) was developed, and Consolidator (grant no. 682068-PRESTISSIMO), awarded to further develop Vlasiator and use it for scientific investigations. The authors gratefully acknowledge the Academy of Finland grant nos. 312351, 309937, 328893, 322544, and 339756, and the Horizon 2020 FRoST grant no. 704681. The CSC–IT Center for Science in Finland and the PRACE Tier-0 supercomputer infrastructure in HLRS Stuttgart (grant nos. PRACE-2012061111 and PRACE-2014112573) are acknowledged as they made these results possible.

References

Archer, M. O., & Horbury, T. S. (2013). Magnetosheath dynamic pressure enhancements: Occurrence and typical properties. *Annales Geophysicae*, *31*(2), 319–331. https://doi.org/10.5194/angeo-31-319-2013

Archer, M. O., Horbury, T. S., & Eastwood, J. P. (2012). Magnetosheath pressure pulses: Generation downstream of the bow shock from solar wind discontinuities. *Journal of Geophysical Research*, *117*(A5). https://doi.org/10.1029/2011JA017468

Battarbee, M., Ganse, U., Pfau-Kempf, Y., Turc, L., Brito, T., Grandin, M., et al. (2020). Non-locality of Earth's quasi-parallel bow shock: Injection of thermal protons in a hybrid-Vlasov simulation. *Annales Geophysicae*, *38*(3), 625–643. https://doi.org/10.5194/angeo-38-625-2020

Battarbee, M., Hannuksela, O. A., Pfau-Kempf, Y., Alfthan, S. V., Ganse, U., Jarvinen, R., & Grandin, M. (2021). *Fmihpc/analysator: V0.9* (Vol. 9). Zenodo. https://doi.org/10.5281/ZENODO.4462515

Dimmock, A. P., Nykyri, K., & Pulkkinen, T. I. (2014). A statistical study of magnetic field fluctuations in the dayside magnetosheath and their dependence on upstream solar wind conditions. *Journal of Geophysical Research: Space Physics*, *119*(8), 6231–6248. https://doi.org/10.1002/2014JA020009

Eastwood, J. P., Lucek, E. A., Mazelle, C., Meziane, K., Narita, Y., Pickett, J., & Treumann, R. A. (2005). The Foreshock. *Space Science Reviews*, *118*(1), 41–94. https://doi.org/10.1007/s11214-005-3824-3

Gutynska, O., Sibeck, D. G., & Omidi, N. (2015). Magnetosheath plasma structures and their relation to foreshock processes. *Journal of Geophysical Research: Space Physics*, *120*(9), 7687–7697. https://doi.org/10.1002/2014JA020880

Hietala, T. V., Andréeová, K., Vainio, R., Vaivads, A., Palmroth, M., Rème, H., et al. (2009). Supermagnetosonic Jets behind a collisionless quasiparallel shock. *Physical Review Letters*, *103*(24), 245001. https://doi.org/10.1103/PhysRevLett.103.245001

Hoppe, M. M., Russell, C. T., Frank, L. A., Eastman, T. E., & Greenstadt, E. W. (1981). Upstream hydromagnetic waves and their association with backstreaming ion populations: ISEE 1 and 2 observations. *Journal of Geophysical Research*, *86*(A6), 4471–4492. https://doi.org/10.1029/JA086iA06p04471

Karimabadi, H., Roytershteyn, V., Vu, H. X., Omelchenko, Y. A., Scudder, J., Daughton, W., et al. (2014). The link between shocks, turbulence, and magnetic reconnection in collisionless plasmas. *Physics of Plasmas*, *21*(6), 062308. https://doi.org/10.1063/1.4882875

Karlsson, T., Kullen, A., Liljeblad, E., Brenning, N., Nilsson, H., Gunell, H., & Hamrin, M. (2015). On the origin of magnetosheath plasmoids and their relation to magnetosheath jets. *Journal of Geophysical Research: Space Physics*, *120*(9), 7390–7403. https://doi.org/10.1002/2015JA021487

Lucek, E. A., Horbury, T. S., Balogh, A., Dandouras, I., & Rème, H. (2004). Cluster observations of structures at quasi-parallel bow shocks. *Annales Geophysicae*, *22*(7), 2309–2313. https://doi.org/10.5194/angeo-22-2309-2004

Lucek, E. A., Horbury, T. S., Dandouras, I., & Rème, H. (2008). Cluster observations of the Earth's quasi-parallel bow shock. *Journal of Geophysical Research*, *113*(A7). https://doi.org/10.1029/2007JA012756

Lucek, E. A., Horbury, T. S., Dunlop, M. W., Cargill, P. J., Schwartz, S. J., Balogh, A., et al. (2002). Cluster magnetic field observations at a quasi-parallel bow shock. *Annales Geophysicae*, *20*(11), 1699–1710. https://doi.org/10.5194/angeo-20-1699-2002

Němeček, Z., Šafránková, J., Přech, L., Sibeck, D. G., Kokubun, S., & Mukai, T. (1998). Transient flux enhancements in the magnetosheath. *Geophysical Research Letters*, *25*(8), 1273–1276. https://doi.org/10.1029/98GL50873

Omelchenko, Y. A., Chen, L.-J., & Ng, J. (2021). 3D space-time adaptive hybrid simulations of magnetosheath high-speed jets. *Journal of Geophysical Research: Space Physics*, *126*, e2020JA029035. https://doi.org/10.1029/2020JA029035

Omidi, N., Berchem, J., Sibeck, D., & Zhang, H. (2016). Impacts of spontaneous hot flow anomalies on the magnetosheath and magnetopause. *Journal of Geophysical Research: Space Physics*, *121*(4), 3155–3169. https://doi.org/10.1002/2015JA022170

Palmroth, M., Ganse, U., Pfau-Kempf, Y., Battarbee, M., Turc, L., Brito, T., et al. (2018). Vlasov methods in space physics and astrophysics. *Living Reviews in Computational Astrophysics*, *4*(1), 1. https://doi.org/10.1007/s41115-018-0003-2

Palmroth, M., Hietala, F., Archer, M., Karlsson, T., Blanco-Cano, X., Turc, L., et al. (2018). Magnetosheath jet properties and evolution as determined by a global hybrid-Vlasov simulation. *Annales Geophysicae*, *36*(5), 1171–1182. https://doi.org/10.5194/angeo-36-1171-2018

Palmroth, M., Raptis, S., Suni, J., Karlsson, T., Turc, L., Johlander, A., et al. (2021). Magnetosheath jet evolution as a function of lifetime: Global hybrid-Vlasov simulations compared to MMS observations. *Annales Geophysicae*, *39*(2), 289–308. https://doi.org/10.5194/angeo-39-289-2021

Pfau-Kempf, Y., Von Alfthan, S., Sandroos, A., Ganse, U., Koskela, T., Battarbee, M., & Alho, M. (2021a). *Fmihpc/vlasiator: Vlasiator5.1*. Zenodo. https://doi.org/10.5281/ZENODO.4719554

Pfau-Kempf, Y., Von Alfthan, S., Sandroos, A., Ganse, U., Koskela, T., Battarbee, M., & Alho, M. (2021b). *Vlasiator simulation data (runs ABA, ABC, AEA, AEC)*. University of Helsinki. Retrieved from http://urn.fi/urn:nbn:fi:att:b508942a-ffc0-4e21-8b8b-b91fcfdbd6ee

Plaschke, F., Hietala, H., & Angelopoulos, V. (2013). Anti-sunward high-speed jets in the subsolar magnetosheath. *Annales Geophysicae*, *31*(10), 1877–1889. https://doi.org/10.5194/angeo-31-1877-2013

Plaschke, F., Hietala, H., Angelopoulos, V., & Nakamura, R. (2016). Geoeffective jets impacting the magnetopause are very common. *Journal of Geophysical Research: Space Physics*, *121*(4), 3240–3253. https://doi.org/10.1002/2016JA022534

Plaschke, F., Hietala, M., Blanco-Cano, X., Kajdic, P., Karlsson, T., Sibeck, D., et al. (2018). Jets downstream of collisionless shocks. *Space Science Reviews*, *214*(5), 81. https://doi.org/10.1007/s11214-018-0516-3

Plaschke, F., Hietala, H., & Vörös, Z. (2020). Scale sizes of magnetosheath jets. *Journal of Geophysical Research: Space Physics*, *125*(9), e2020JA027962. https://doi.org/10.1029/2020JA027962

Raptis, S., Karlsson, T., Plaschke, F., Kullen, A., & Lindqvist, P.-A. (2020). Classifying Magnetosheath jets using MMS: Statistical properties. *Journal of Geophysical Research: Space Physics*, *125*(11), e2019JA027754. https://doi.org/10.1029/2019JA027754

Rojas-Castillo, D., Blanco-Cano, X., Kajdič, P., & Omidi, N. (2013). Foreshock compressional boundaries observed by Cluster. *Journal of Geophysical Research: Space Physics*, *118*(2), 698–715. https://doi.org/10.1029/2011JA017385

Schwartz, S. J., Burgess, D., Wilkinson, W. P., Kessel, R. L., Dunlop, M., & Luehr, H. (1992). Observations of short large-amplitude magnetic structures at a quasi-parallel shock. *Journal of Geophysical Research*, *97*, 4209–4227. https://doi.org/10.1029/91JA02581

Turc, L., Ganse, U., Pfau-Kempf, Y., Hoilijoki, S., Battarbee, M., Juusola, L., et al. (2018). Foreshock properties at typical and enhanced interplanetary magnetic field strengths: Results from hybrid-Vlasov simulations. *Journal of Geophysical Research: Space Physics*, *123*(7), 5476–5493. https://doi.org/10.1029/2018JA025466

Vuorinen, L., Hietala, H., & Plaschke, F. (2019). Jets in the magnetosheath: IMF control of where they occur. *Annales Geophysicae*, *37*(4), 689–697. https://doi.org/10.5194/angeo-37-689-2019

Wilson, L. B., Sibeck, D. G., Breneman, A. W., Contel, O. L., Cully, C., Turner, D. L., et al. (2014). Quantified energy dissipation rates in the terrestrial bow shock: 1. Analysis techniques and methodology. *Journal of Geophysical Research: Space Physics*, *119*(8), 6455–6474. https://doi.org/10.1002/2014JA019929

Winterhalter, D., & Kivelson, M. G. (1988). Observations of the Earth's bow shock under high Mach number/high plasma beta solar wind conditions. *Geophysical Research Letters*, *15*(10), 1161–1164. https://doi.org/10.1029/GL015i010p01161